Manufacturing Science and Engineering Conference
MSEC 2018
June 18-22, 2018, Texas A&M University, College Station, Texas, USA

MSEC2018-6470

IN-PROCESS MONITORING OF MATERIAL CROSS-CONTAMINATION IN LASER POWDER BED FUSION

Mohammad Montazeri
Mechanical and Materials Engineering Department
Lincoln, Nebraska, United States

Reza Yavari
Mechanical and Materials Engineering Department
Lincoln, Nebraska, United States

Prahalada Rao
Mechanical and Materials Engineering Department
Lincoln, Nebraska, United States

Paul Boulware
Edison Welding Institute (EWI),
Columbus, Ohio, United States

Abstract. The goal of this work is to detect the onset of material cross-contamination in laser powder bed fusion (L-PBF) additive manufacturing (AM) process using data from in-situ sensors. Material cross-contamination refers to trace foreign materials that may be introduced in the powder feedstock used in the process due to reasons, such as poor cleaning of the AM machine after previous builds, or inadequate quality control during production and storage of the feedstock powder material. Material cross-contamination may lead to deleterious changes in the microstructure of the AM part and consequently affect its functional properties. Accordingly, the objective of this work is to develop and apply a spectral graph theoretic approach to detect the occurrence of material cross-contamination in real-time during the build using in-process sensor signatures, such as those acquired from a photodetector. To realize this objective Inconel alloy 625 test parts were made on a custom-built L-PBF apparatus integrated with multiple sensors, including a photodetector (300 nm to 1100 nm). During the process the powder bed was contaminated with two types of foreign materials, namely, tungsten and aluminum powders under varying degrees of severity. Offline X-ray Computed Tomography (XCT) and metallurgical analyses indicated that contaminant particles may cascade to over eight subsequent layers of the build, and enter up to three previously deposited layers. This research takes the first-step towards detecting cross-contamination in AM by tracking the process signatures from the photodetector sensor hatch-by-hatch invoking spectral graph transform coefficients. These coefficients are subsequently traced on a Hoteling T^2 statistical control chart. Using this approach, instances of Type II statistical error in detecting the onset of material cross-contamination was 5% in the case of aluminum, in contrast, traditional stochastic time series modeling approaches, e.g., ARMA had corresponding error exceeding 15%.

Keywords. Additive Manufacturing, Laser Powder Bed Fusion, Inconel 625, Material Cross-Contamination, Real-time Monitoring, Photodetector, Spectral Graph Theory, Qualify-as-you-build.

1 Introduction

1.1 Motivation

Powder Bed Fusion (PBF) is the AM process of choice for making metal parts. Recent studies in the aerospace industry have demonstrated that the PBF AM process can drastically reduce the so-called *buy-to-fly* ratio, which is the ratio of the material that is required to make a part to the final weight of the part. The buy-to-fly ratio is typically 20:1 for traditional subtractive and formative processes, while in the case of metal AM this ratio can be as small as 2:1. Simultaneously, the lead time for delivering a new part design can be shortened from five months to less than a week [1]. This unprecedented flexibility in design and manufacturing has the potential to revolutionize strategic industries, such as aerospace and biomedical.

Despite these possibilities, the poor consistency of AM parts hinders their wider adoption for making mission-critical components. Particularly, the presence of defects in AM parts, such as porosity and geometric distortion, deleteriously affect their functional properties, e.g., fatigue life and strength [2, 3]. Unlike traditional manufacturing processes, given the layered nature of AM, defects may form at any layer and become permanently sealed in by subsequent layers if they are not detected and averted promptly. Hence, there is a need to monitor the integrity of each layer as it is being built to ensure compliance [4].

In the context of quality assurance in AM, the current practice is to examine the part after it is built using X-ray computed tomography (XCT), which is exceedingly expensive and cumbersome. In a recent review article, Seifi *et al.* attest that given the small batch sizes and time required for production, statistical qualification of AM parts based on destructive materials testing may amount to millions of dollars and take over a decade to complete, and is therefore impractical [5].

However, if a sensor data record exists to attest the integrity of every layer, and if this data can be correlated back to the XCT for a few test parts, then this recorded sensor data for each layer, instead of XCT scanning and destructive analysis, can be used to rapidly qualify the part quality, leading to a so-called *qualify-as-you-build* paradigm in AM [6].

1.2 Objectives

As a first-step towards the long-term aim of qualify-as-you-build in AM, the goal of this work is to detect the onset of material contamination-related anomalies in L-PBF. In pursuit of this goal, the objective is to develop and apply a spectral graph theoretic approach for real-time detection of material cross-contamination using in-process sensor signatures acquired by a photodetector. The central hypothesis is that tracking the signatures acquired from the photodetector in the spectral graph domain leads to early and more accurate detection of material cross-contamination in L-PBF, compared to the traditional stochastic delay-embedded time series analysis of the signal, such as autoregressive (AR) and autoregressive moving average (ARMA) modeling.

Current research in this area focuses extensively on defects, such as porosity or distortion which result from factors related to poor choice of process parameters, machine calibration, part design, material, support structures, and part orientation [7, 8]. However, detection of subtler process drifts, such as material cross-contamination, which has been shown to cause variation in the microstructure and functional properties, remains to be investigated [9]. The initiation of contamination-related defects in L-PBF can be traced to: (a) poor quality control of the material feedstock during production and storage, and (b) inadequacies and lapses in the procedures used to purge trace material from the AM machine or powder recovery equipment.

To put the challenge of cross-contamination in pictorial context, Figure 1 shows optical images of an etched Inconel 625 sample contaminated with tungsten and aluminum material. The following inferences can be drawn from this experimental result, which will be described further in depth in Sec. 2.

- Figure 1(a): Contamination with tungsten manifests as unfused particles (light hued inclusions in the darker Inconel 625 matrix). This is because the melting point of tungsten is much higher (3422 °C) than Inconel 625 (~1300 °C). In a recent publication, Brandão *et al.* hypothesize that given the hardness of tungsten, unmelted tungsten particles tend to become preferred sites for crack initiation under tensile loading [9]. At higher magnification the tungsten contaminant particles are seen to cascade over subsequent layers.
- Figure 1(b): Contamination with aluminum does not manifest in clearly distinguishable particle traces, however it tends to distort the meltpool.

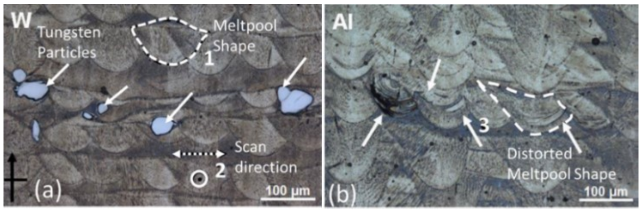

Figure 1: Optical image of an etched and polished Inconel 625 specimen. The black arrow indicates the build direction. (a) Contamination with Tungsten, which due to its high melting point does not fuse, and tends to cascade through several layers. The dashed-line (1) indicates the shape of a molten pool, penetrated into the previously deposited layer. Also, the overlaps between tracks could be recognized. The dashed line and circle (2) shown at the bottom of the tungsten specimen are representative of the hatching directions in the two consecutive layers. (b) The contamination with aluminum is not readily evident as trace particles, but closer examination of the hatch pattern reveals that aluminum tends to distort the meltpool as indicated by the arrows (3).

These images demonstrate that material cross-contamination changes the basic microstructure of the build, and has the proclivity to spread beyond the layer in which they occur. This work addresses the following open research question in the context of material cross-contamination in L-PBF process − what process signatures can capture the onset of contamination? This is an important area of research, which is at the crux of the current repeatability and reliability-related challenges in AM and will ultimately set the stage for a qualify-as-you-build paradigm in AM.

The rest of this paper is organized is follows the experimental setup is described in Sec. 2, the spectral graph theoretic approach is explained and applied to the L-PBF process signals in Sec. 3, followed by conclusions and avenues for future work in Sec. 4.

2 Experimental Setup

2.1 Customized Test Bed and Data Acquisition

In this research, a customized, open architecture L-PBF system was designed and implemented at Edison Welding Institute (EWI) [10]. An array of heterogeneous sensors is integrated within the apparatus, and are located on an optical table near the laser scanning mechanism. Further details of this setup are available in Ref [10]. To precisely control the degree of material contamination, a material dispensing setup was fabricated. The setup attaches to the recoater arm and powder material (contaminant) is dispensed from a motorized hopper. Figure 2 shows the schematic illustration of the sensor test bed and the equipment used for contaminant dispersion.

An Inconel 625 cuboid-shaped test part of size 10 mm × 10 mm × 15.20 mm (height) was built with the following parameters after extensive offline studies studies: scan velocity (V) 960 mm/s, laser power (P) 270 W, layer thickness (T) 0.040 mm, and hatch spacing (H) 0.1 mm, i.e., an applied volumetric energy density ($E_V = P/(H \times V \times T)$) ≈ 70 J/mm^3. The experimental procedure for dispersing contaminants, namely aluminum (Al) and tungsten (W), is depicted in Figure 3. The contaminants are dispersed over the powder bed every 20th layer.

Photodetector signal data is acquired for total of 10 layers as follows: (1) two layers prior to contamination, (2) the contaminated layer, and (3) seven layers subsequent to the contamination. This procedure for purposely introducing contamination was repeated 3 times over a total build consisting of 380 layers. The severity of contamination is controlled at three levels for each type of contaminant material (viz., aluminum and tungsten). Further, the contaminant is distributed over the powder bed in two ways, called dynamic contamination and static contamination.

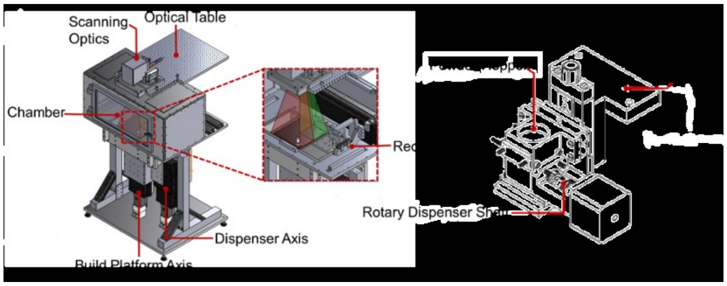

Figure 2: A schematic representation of the (a) L-PBF platform and (b) fixture made by EWI to deliver metered amount of contamination [10].

In static contamination, which occurs in levels labeled L_1, L_2, and L_3, the contaminant material is dispensed entirely in one area with the recoater stopped. In the so-called dynamic contamination mode, the contaminant powder is dispensed synchronous with the recoater movement. That is, the hopper motor in the fixture shown in Figure 2(b) is continually operational as the recoater rakes the Inconel powder across the bed. This sort of deposition of the contaminant results in an elongated line or streak across the powder bed, and is labeled L_4, L_5 and L_6 in ascending order of severity. The consequence of the different types of contamination types is captured using an in-process optical camera in Figure 4(a_1) and (a_2); the severity of the contamination levels and their sequence within each replicate of experiment are further detailed in Figure 4(b_1) and (b_2). To minimize the eventuality of powder leakage, the whole test bed including dispenser, build plate, and collector was sealed. After testing the system for 100 times, no leakage of powder is detected from the powder container on the build platform and collector.

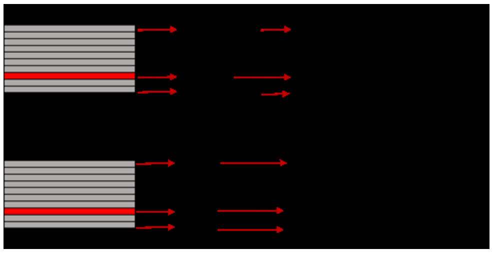

Figure 3: The manner in which contamination is introduced during the build. The gray layers show the ones where data is captured. The red layers indicate where the contamination is introduced.

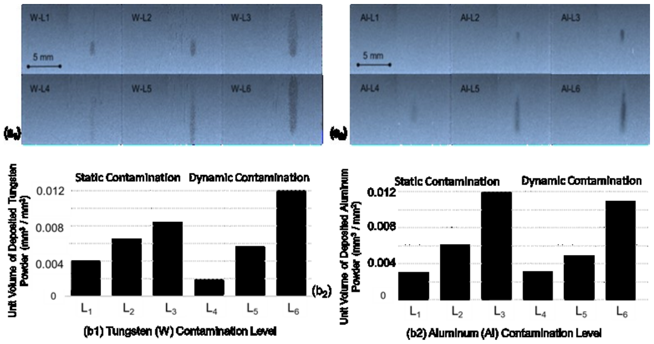

Figure 4: Post recoating optical images after contamination with (a_1) Tungsten and (a_2) Aluminum. The unit volumes of deposited powders for each of six contamination levels in (b_1) tungsten and (b_2) aluminum.

The photodetector sensor utilized in this study was a Thorlabs model PDA36A and is coaxial and synchronized with the switching of the laser, i.e., data is acquired only when the laser is active. The analog photodetector signal is acquired via National Instruments NI 9215 analog input module. The detection range of the photodetector is the 350 nm to 1100 nm range with the gain of 40 dB, and the sampling rate is set at 10 KHz. The data is acquired hatch-by-hatch; the laser traces hatch pattern alternating parallel for odd layers, and perpendicular for even layers. The hatch pattern information will be used later in Sec. 3.2 to relate the sensor signatures to the position at which the contamination occurs in XCT. In all, data is available for 180 of the total 380 layers. Each layer is comprised of 100 hatches, and each hatch takes ~ 0.01 sec. (10 milliseconds) to melt noting that the laser scan velocity is 960 mm/sec. Hence there are 100 photodetector data points acquired per hatch given that the sensor sampling rate is 10 KHz. In this build the laser stays on for ~ 1 sec. per layer, and for a total of under 7 minutes counting the time to melt the contour. The photodetector signal related to the six level of tungsten and aluminum contamination for one iteration are shown in Figure 5(a) and (b), respectively. The layers contaminated with tungsten portray significant peaks. However, such a clear change is not apparent in the photodetector signal for the aluminum contamination case.

Table 1: The build layout and contamination pattern. The contamination set of L_1 through L_6 was deposited three times, and in the end of 3 iterations was followed by 20 cover layers.

Contamination Set #	Base Line (BL) / Contamination Layer (L_n, n=1 to 6)	Start Layer	End Layer	End Height (mm)
Iteration 1	BL	1	19	0.76
	L_1 -1	20	20	0.80
	BL	21	39	1.56
	L_2 -1	40	40	1.60
	BL	41	59	2.36
	L_3 -1	60	60	2.40
	BL	61	79	3.16
	L_4-1	80	80	3.20
	BL	81	99	3.96
	L_5-1	100	100	4.00
	BL	101	119	4.76
	L_6-1	120	120	4.80
× 2 iterations of the build pattern)	BL- L_6 -2 BL- L_6 -3	121	360	14.44
Cover Layers	BL	361	380	15.20

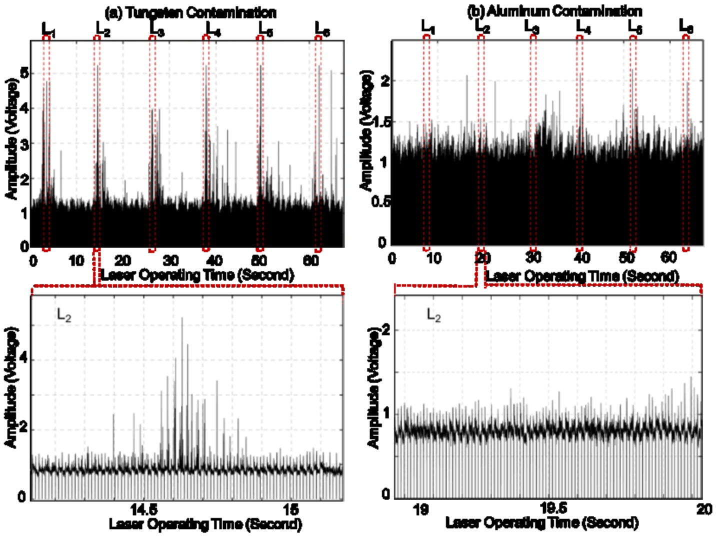

Figure 5: (top row) The photodetector signal associated with the six level of (a) Tungsten contamination and (b) Aluminum contamination in Inconel 625. (bottom row) The second contamination level (L_2) is magnified and the signal corresponding to tungsten contamination has clear spikes compared to aluminum.

3.2 Offline X-Ray Computed Tomography (XCT) Analysis of the Build

The aim of this section is to understand the effect of contamination on the structure of the build. To realize this aim, the specimen is examined using X-Ray Computed Tomography (XCT) along the various cutting planes demarcated in Figure 6. The vertical and horizontal cross sections of the 3D volume captured for the tungsten contaminated specimen is shown in Figure 7, wherefrom the contaminant powder is clearly discerned.

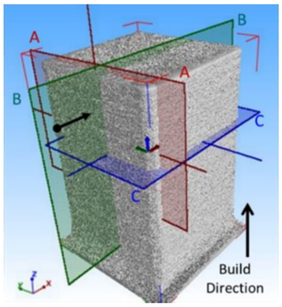

Figure 6: Three-dimensional (3D) reconstruction of the specimen contaminated with tungsten powder particles. The powder recoating moves along the X-axis direction.

Figure 7(a) shows the XCT across the vertical cross-section (Y-Z plane, cutting plane A-A as depicted in Figure 7) of the test artifact. Observed in Figure 7(a) are the contaminated layers over three replicates. Closer examination of these vertical cross-sections reveals that for high tungsten contamination levels, such as L_3, the tungsten particles disperse up to three layers preceding the layer in which they are introduced, and as much as eight subsequent layers. In other words, contamination tends to cascade across layers, and influences the structure of both the preceding and subsequent deposition. This assertion is further corroborated through metallurgical analysis in Figure 8.

Similarly, Figure 7 (b) shows the effect of contamination as viewed along the X-Z direction (cutting plane B-B); Figure 7 (c) is the cross-section taken along the X-Y direction (cutting plane C-C). We note that in Figure 7(a) and (b), due to procedural lapses during XCT scanning. the second level of tungsten contamination (L_2) for the first iteration was not captured. This missing data is demarcated by a star in Figure 7(a) and (b).

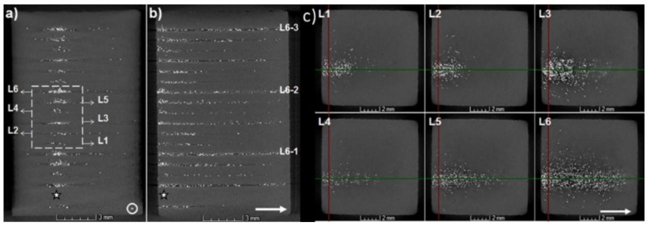

Figure 7: The cross sectional views of the specimen contaminated by the Tungsten powder particles, a) vertical cross section normal to the recoating direction (cutting plane A-A, Y-Z direction), b) vertical cross section along the recoating direction (cutting plane B-B, X-Z direction) c) horizontal cross section (cutting plane C-C, X-Y direction).

The specimen with embedded tungsten contaminant was sectioned and primary etched with an alcohol-based Kalling's solution. The specimens were secondary etched using a 10% chromic acid solution at 2.4 volts. In the optical micrograph of the etched sample shown in Figure 8(a) the presence of tungsten contaminants in the Inconel 625 matrix is evident. More remarkably, tungsten particle traces are observed not just in the layer they are introduced, but also over multiple layers – both preceding and subsequent layers. The spread of contaminants to layers beyond which they are introduced is hypothesized as the effect of the repeated remelting of the material. However, modeling of the meltpool dynamics is required for confirming this effect. Recent computational modeling work at Lawrence Livermore National Laboratories by King *et al.* towards simulating the meltpool dynamics shows that material reflow and remelting influences the structure of the previous layers, and may even be used beneficially to control and mitigate defects, such as porosity [11]. Further investigation in this direction to elucidate how and why material contamination cascades across layers is beyond the scope of this work.

The cascading effect of contamination is further verified in the XCT observations in Figure 8(b). The XCT cross-section in Figure 8(b) is taken in the X-Y plane, the label *n* refers to the layer in which contamination is introduced, *n-1* is the immediate preceding layer, *n-2* is two layers prior, and so on; similarly a plus sign is used to indicate layers subsequent to layer *n*.

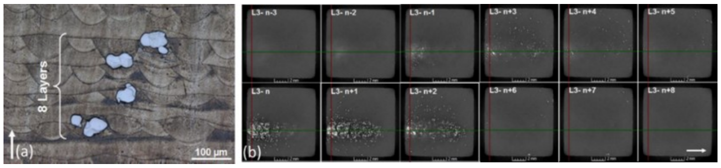

Figure 8: The optical micrograph of a tungsten contaminated specimen with tungsten particles observed over 8 layers. (b) XCT images in the horizontal plane section (cutting plane C-C, X-Y direction) for the L_3 severity level shows that trace tungsten particles persist over eight subsequent layers and penetrate through three preceding layers.

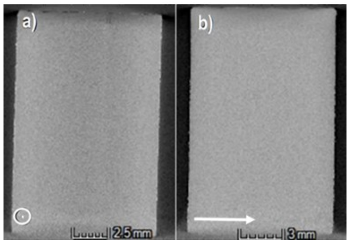

Figure 9: The cross sectional views of the specimen contaminated by the Aluminum powder particles, a) vertical cross section normal to the recoating direction (cutting plane A-A, Y-Z direction), b) vertical cross section along the recoating direction (cutting plane B-B, X-Z direction).

In the context of aluminum contamination, Figure 9 shows the vertical cross sections of the specimen; aluminum trace particles were not detected with XCT, but as first shown in Figure 1(b_2), the meltpool in the etched sample where aluminum contamination occurs is distorted. The subsequent section, Sec. 3 develops and applies a spectral graph theoretic approach to capture these instances of contamination during the build using data from the photodetector.

3 Spectral Graph Theory and its Application to Detection of Material Cross-Contamination in L-PBF

The aim of this section is to detect the onset of material cross-contamination in L-PBF process using in-process data. To realize this aim, the key idea is to transform the raw data into a domain that makes it tractable to extract signatures in real-time. In this work, the signal transformation procedure adopted is from the area of spectral graph theory, and has been discussed in depth in our previous research [12]. The novelty herein is to focus on one signal hatch - specified as the single line printed by the laser- and extract the sensor signatures using spectral graph theory.

The procedure is summarized in Figure 10, and encapsulates the four key steps. Steps 1 through 3 can be considered as the training phase, wherein a library of sensor signatures representing non-contaminated states is created. The last step, Step 4 classifies an unknown signal into one of the two states (contaminated vs. non-contaminated) in real-time within a control chart framework. The underlying concept for each step is summarized herewith. The mathematical convention is to denote matrices and vectors in bold.

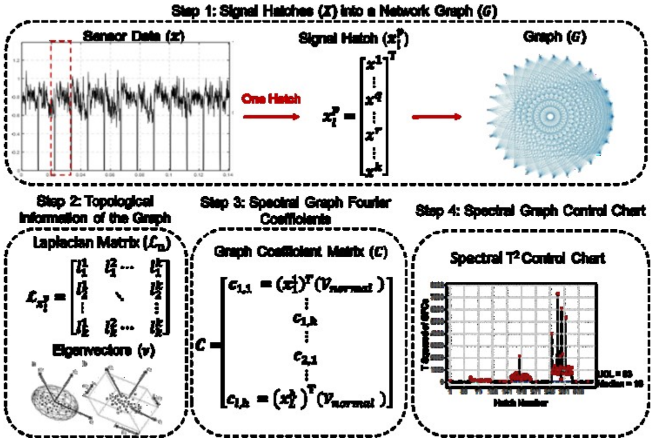

Figure 10: Graphical overview of the proposed spectral graph theoretic approach for detecting material contamination.

Step 1: The photodetector signal $\boldsymbol{x}_l^p$ representing each hatch $p \in \{1 \dots h\}$ at layer $l \in \{1 \dots L\}$ of the melting process is converted into a weighted and undirected network graph $G \equiv (V, E, W)$.

Step 2: The topological information in the graph $G \equiv (V, E, W)$ is extracted in terms of the eigenvectors $(\boldsymbol{v}_{x_1^p})$ and eigenvalues $(\lambda_{x_1^p})$ of the Laplacian matrix $(\boldsymbol{\mathcal{L}}_{x_1^p})$. In other words, a spectral graph transform $G(\cdot)$ on the signal $\boldsymbol{x}_1^p$ is defined, i.e., $G(\boldsymbol{x}_1^p) \rightarrow \boldsymbol{\mathcal{L}}_{x_1^p}(\lambda_{x_1^p}, \boldsymbol{v}_{x_1^p})$.

Step 3: A learning procedure is used to obtain a universal eigenvector basis $\boldsymbol{V}_{normal}$ corresponding to the normal or non-contaminated process state. Through this universal basis a spectral graph Fourier transform $\hat{G}(\boldsymbol{x}_l^p) = \left[(\boldsymbol{x}_l^p)^T (\boldsymbol{\mathcal{V}}_{normal})\right]$ is defined. Such a graph-based Fourier transform facilitates creating a library of spectral graph coefficients $\boldsymbol{C}$ archetypical of the non-contaminated process state.

Step 4: The coefficients $\boldsymbol{C}$ representative of the normal or non-contaminated process state are used to build a multivariate statistical control chart, called the Hoteling T^2 control chart. Given a new signal $\boldsymbol{y}$ an inner product with the basis vector $\boldsymbol{\mathcal{V}}_{normal}$, $\hat{G}(\boldsymbol{y}) = [(\boldsymbol{y})^T(\boldsymbol{\mathcal{V}}_{normal})]$, leads to a set of new spectral graph Fourier coefficients $\hat{G}(\boldsymbol{y})$ that are easily traced on the control chart. If $\hat{G}(\boldsymbol{y})$ falls outside the control limits it is deemed as belonging to an out-of-control state, i.e., in this work the data is presumably from a layer contaminated with trace materials.

3.1 The Spectral Graph Theoretic Approach for Analyzing Signals in Real-time

Step 1: Converting the photodetector signal hatch-by-hatch into a network graph.

In this step, the aim is to represent each hatch related to the photodetector sensor data $\boldsymbol{x}$ as a weighted, undirected network $G(V, E, W)$. Where V, E and W are the graph vertices, edges and weight between the edges, respectively. This graph $G(V, E, W)$ is a lower dimensional representation of the signal $\boldsymbol{x}$.

Consider a *m*-data point long 1-dimensional signal $\boldsymbol{x}$ for a layer $l \in \{1 \dots L\}$ per the matrix shown in Eqn. (1). In this work L = 180 (data from ten layers for each of the six levels of contamination replicated thrice, 10 × 6 × 3).

$$\boldsymbol{x}_l = [x^1 \quad \dots \quad x^i \quad \dots \quad x^m]^{\mathrm{T}}, l \in \{1 \dots L\} \tag{1}$$

Each layer is comprised of *h* hatches, in this work *h* = 100, *m* = 10,000. Thus, the signal $\boldsymbol{x}_l$ is further divisible into the corresponding *h* hatches, each hatch has *k* data points, with *k* = 100. This information was obtained by tracking the on-off switching time of the laser in each layer, i.e., the time between when the laser goes on and off relates to one hatch. Let each hatch in a layer be defined as a matrix $\boldsymbol{x}_l^p$, $p \in \{1 \dots h\}$, $l \in \{1 \dots L\}$, where *h* (=100) is the number of hatches per layer and *L* (=180) is the number of layers, so that it can be written in matrix form as,

$$\boldsymbol{x}_l^p = [x^1 \quad \dots \quad x^q \quad \cdots \quad x^r \quad \dots \quad x^k]^{\mathrm{T}} \tag{2}$$

To transform a signal of each hatch into a network graph, the following procedure is followed. First, the pairwise comparisons $\mathscr{w}_{qr}$ is computed using a kernel function Ω [13] per Eqn. (3), where x^q and x^r are two points of signal for hatch $\boldsymbol{x}_l^p$

$$\mathscr{w}_{qr} = \Omega(x^q, x^r)\ \forall\, q, r \in (1 \cdots k). \tag{3}$$

While different types of kernel functions Ω, such as the radial basis or Mahalanobis can be defined to obtain the graph G. For simplicity, in this work we use the standardized Euclidean kernel shown in Eqn. (4), where V is the variance of the signal $\boldsymbol{x}_l^p$.

$$\mathscr{w}_{qr} = (x^q - x^r)V^{-1}(x^q - x^r) \tag{4}$$

The symmetric *similarity matrix* $\boldsymbol{S}^{k \times k} = [\mathscr{w}_{qr}]$ represents a weighted and undirected network graph G; each row and column of $\boldsymbol{S}^{k \times k}$ is the vertex V (or node) of the graph, the relationship between two nodes is indexed by edges, in terms of its connection status E and weight W. The graph is then represented as $G \equiv (V, E, W)$ [14]. To be more specific we make the following notational additions to the similarity matrix $\boldsymbol{S}$ and graph G: $\boldsymbol{S}_{x_l^p}$; $G_{x_l^p}$, where $\boldsymbol{x}_l^p$ relates to a specific hatch p for the signal related to the layer *l*.

Step 2: Extracting topological information for the graph surface

This phase aims to extract topological information from the graph G. Once the data $\boldsymbol{x}_l^p$ in a particular hatch is represented as a graph $G_{x_l^p}$, the Laplacian Eigenvectors $\boldsymbol{v}_{x_l^p}$ are computed. This topological information is subsequently used to capture the process drifts from the nominal condition. From $\boldsymbol{x}_l^p$, the *degree* d_q of a node q, $q = \{1 \dots k\}$ is computed, which is a count of the number of edges that are incident upon the node. The node degree is the sum of each row in the similarity matrix $\boldsymbol{S}^{k \times k}$ and the diagonal *degree matrix* $\boldsymbol{\mathcal{D}}$ is structured from d_q as follows,

$$d_q = \sum_{r=1}^{k} w_{qr}\ \forall\, q = \{1 \dots k\} \tag{5}$$

$$\boldsymbol{\mathcal{D}}^{k \times k} \overset{\text{def}}{=} \operatorname{diag}(d_1, \cdots, d_k). \tag{6}$$

This leads to the normalized Laplacian $\boldsymbol{\mathcal{L}}$ of the graph G, which is defined as,

$$\boldsymbol{\mathcal{L}} \overset{\text{def}}{=} \boldsymbol{\mathcal{D}}^{-\frac{1}{2}} \times (\boldsymbol{\mathcal{D}} - \boldsymbol{S}) \times \boldsymbol{\mathcal{D}}^{-\frac{1}{2}},$$
$$\text{where, } \boldsymbol{\mathcal{D}}^{-\frac{1}{2}} = \operatorname{diag}\left(1 \Big/ \sqrt{d_1}, \cdots, 1 \Big/ \sqrt{d_k} \right). \tag{7}$$

Thereafter, the Eigen spectrum of $\boldsymbol{\mathcal{L}}$ is computed as,

$$\boldsymbol{\mathcal{L}}\boldsymbol{v} = \lambda \boldsymbol{v}. \tag{8}$$

At the end of step 2, we have essentially defined a spectral graph transform on a signal $\boldsymbol{x}_l^p$;

$$G(\boldsymbol{x}_l^p) \to \boldsymbol{\mathcal{L}}_{x_l^p}(\lambda_{x_l^p}, \boldsymbol{v}_{x_l^p}). \tag{9}$$

In other words, we have transformed the signal $\boldsymbol{x}_l^p$ for a specific hatch in terms of the eigenvectors ($\boldsymbol{v}$) and eigenvalues ($\lambda_{x_l^p}$) of its Laplacian matrix ($\boldsymbol{\mathcal{L}}_{x_l^p}$).

Step 3: Building the signal basis and spectral transformation

This step aims to obtain the eigenvectors of $\boldsymbol{\mathcal{L}}_{x_1^p}$ across all non-contaminated hatches and converge it towards a universal eigenvector basis. In other words, we want to represent the signal during the non-contaminated state in terms of a single or universal eigenvector represented as $\boldsymbol{\mathcal{V}}_{normal}$.

Step 3.1: A single universal basis $\boldsymbol{\mathcal{V}}_{normal}$ is obtained by applying a simple update schema [15]. As the eigenvectors $\boldsymbol{v}_{\boldsymbol{x}_l^p}$, for each hatch is calculated, we update the basis as follows,

$$\begin{gathered}\boldsymbol{\mathcal{V}}_{\boldsymbol{x}_l^{p+1}} = \boldsymbol{\mathcal{V}}_{\boldsymbol{x}_l^p} + \Delta\left(\boldsymbol{v}_{\boldsymbol{x}_l^{p+1}} - \boldsymbol{v}_{\boldsymbol{x}_l^p}\right),\ p \in \{1 \dots h\}, \\ l \in \{1 \dots L\}, \\ \boldsymbol{\mathcal{V}}_{normal} = \boldsymbol{\mathcal{V}}_{\boldsymbol{x}_L^h}\end{gathered} \qquad (10)$$

Initialized with $\boldsymbol{\mathcal{V}}_{\boldsymbol{x}_1^1} = \boldsymbol{v}_{\boldsymbol{x}_1^1}$ with Δ set the to a small value (in our case 0.001). To make the process computationally simpler only a small set of the first 10 non-zero Eigenvectors of the Laplacian $\boldsymbol{\mathcal{L}}_{\boldsymbol{x}_1^p}$ are updated.

Step 3.2: We define the spectral graph transform, which is analogous to the discrete Fourier transform. A spectral graph Fourier transform $\hat{G}(\cdot)$ on a signal hatch $\boldsymbol{x}_l^p$ can be defined as follows [16],

$$\hat{G}(\boldsymbol{x}_l^p) = \left[(\boldsymbol{x}_l^p)^T (\boldsymbol{\mathcal{V}}_{normal})\right] \qquad (11)$$

Applying this inner product through all the non-contaminated layers and hatches by taking the product $(\boldsymbol{x}_l^p)^{\mathrm{T}} \cdot \boldsymbol{\mathcal{V}}_{normal}$, $l = \{1 \dots L\}$, $p \in \{1 \dots h\}$, leads to the graph coefficient matrix $\boldsymbol{C}$.

$$\begin{gathered}\boldsymbol{C} = \Big[\left[(\boldsymbol{x}_1^1)^T (\boldsymbol{\mathcal{V}}_{normal}) = \boldsymbol{c}_{1,1}\right]; \dots \\ \dots; \left[(\boldsymbol{x}_{\mathrm{L}}^p)^{\mathrm{T}} (\mathcal{V}_{normal}) = \boldsymbol{c}_{L,p}\right]\Big]\end{gathered} \qquad (12)$$

Essentially, each term $\boldsymbol{c}_{l,p}$, $l = \{1 \dots L\}, p \in \{1 \dots h\}$, is a matrix that is $1 \times n$ long, where n is the number of Eigenvectors in the universal basis $\boldsymbol{\mathcal{V}}_{normal}$ selected for analysis. Each $\boldsymbol{c}_{l,p}$ can be visualized as a set of output variables which needs to be tracked across the process – they are termed as spectral graph Fourier transform coefficients.

Step 4: Change point detection using spectral graph control chart

This step aims to detect material cross-contamination by tracking the spectral graph transform coefficients $\boldsymbol{c}_{l,p}$. To realize this aim, we use a multivariate statistical control chart called the Hotelling T^2 [17]. The control limit of the chart is constructed based on the so-called *in-control state* which in the context of this work is defined as the non-contaminated signal. For the Hoteling T^2 control chart only the upper control limit needs to be estimated as the lower control limit is zero. The application of the control chart proceeds in two phases, in the first phase (Phase 1) called the training phase, the upper control limit of the chart is constructed based on the spectral graph Fourier coefficients from the non-contaminated state; and in the second phase (Phase 2), called the monitoring phase, the coefficients for incoming signals for each new hatch is tracked on the chart, and their status, i.e., whether they belong to contaminated or non-contaminated state is determined.

Step 4.1: Phase 1 – Training the control chart

In this phase we ascertain the control limits of the chart. Data points within the control limits are said to be *in-control*, which in the context of this work refers to non-contaminated state. The data points falling outside the control limits are termed *out-of-control*. In this research, an out-of-control point is interpreted as the onset of cross-contamination.

For setting the control limits, we only use the photodetector signals from the two layers before the contamination is introduced, and only those from the first iteration of the build. Such an exceedingly conservative strategy towards determining the control limits largely precludes the possibility of introducing signals which might be vitiated, noting that metallurgical analysis revealed that contamination tends to cascade over several subsequent layers.

Accordingly, only 24 of the total 60 layers for which data is available in iteration 1 are used in the training phase, amounting to 2400 hatches. This translates to roughly 15% of the available data for 180 layers used for analysis.

The test statistic, or the point plotted on the control chart is called the T^2 value, and is delineated in Eqn. (13) where $\overline{\boldsymbol{C}}$ is the spectral graph theoretic coefficient matrix mean vector, and S^{-1} is the inverse of the covariance matrix of $\boldsymbol{C}$.

$$T_{l,p}^2 = \left(\boldsymbol{c}_{l,p} - \overline{\boldsymbol{C}}\right)' S^{-1} \left(\boldsymbol{c}_{l,p} - \overline{\boldsymbol{C}}\right) \qquad (13)$$

The upper control limit (UCL) of the chart is calculated using Eqn. (14) where $\beta_{\alpha,n/2,(hL-n-1)/2}$ is the upper α tail of a Beta distribution with parameters n (the number of eigenvectors) and h and L are the number of hatches and number of layers, respectively. The lower control limit of a Hoteling T^2 is set at zero. In this work, we set $\alpha = 0.1\%$.

$$\mathrm{UCL} = \frac{(hL-1)^2}{hL} \beta_{\alpha,n/2,(hL-n-1)/2} \qquad (14)$$

Thereafter, the T^2 values from Eqn. (13) are plotted on the control chart, and the UCL is revised by removing any data points that fall erroneously above it. The re-estimation of the control limit by removing erroneous out-of-control data is only done once, and is called the delete and revise procedure.

Step 4.2: Phase 2 – Using the control chart for monitoring the process

Once the UCL of a chart is determined, the new sensor signatures are plotted upon the chart as follows. Suppose a photodetector signal $\boldsymbol{y}$ is obtained for a hatch, we estimate its graph Fourier coefficients $\hat{G}(\boldsymbol{y})$ as,

$$\hat{G}(\boldsymbol{y}) = [(\boldsymbol{y})^T (\boldsymbol{\mathcal{V}}_{normal})] \qquad (15)$$

The Hoteling T^2 statistic, labeled T_y^2 for this new sensor signature is calculated as follows,

$$T_y^2 = \left(\hat{G}(\boldsymbol{y}) - \overline{\boldsymbol{C}}\right)' S^{-1} \left(\hat{G}(\boldsymbol{y}) - \overline{\boldsymbol{C}}\right) \qquad (16)$$

The T_y^2 value is plotted on the control chart, and if it falls above the UCL, we conclude that contamination has occurred.

We now briefly describe the statistical error measurements that underscore the effectiveness of detecting contamination in the context of a control chart. Control charts are culpable of two types of statistical errors, namely, Type I (α or false alarm) and Type II (β or failing to detect). The Type I error rate is the percentage of data points (each data point on the control chart used in this work represents a hatch) that are falsely categorized as falling above the upper control limit when the process is in-control. In other words, a data point is falsely deemed to indicate contamination, i.e., there is no actual contamination, but the control chart erroneously indicates that contamination has occurred. Conversely, the Type II (β) error rate is the percentage of data points that fall inside the UCL when they should in reality lie outside, i.e., contamination has occurred, but the control chart fails to indicate it because the data point falls inside the control limits. Given a finite amount of data there is a tradeoff involved between Type I and Type II errors.

3.2 Application to Detection of Contamination in L-PBF

In this section, the proposed spectral graph theoretic algorithm is applied to the L-PBF process with the aim of detecting the onset of aluminum and tungsten cross-contamination from the photodetector signals. First, the photodetector signal for the non-contaminated state is apportioned hatch-by-hatch for each layer. This is possible because the laser position is tracked and recorded throughout the build. The photodetector signal for each hatch *p* for layer *l* is denoted as $\boldsymbol{x}_l^p$ in Eqn. (2).

Next, using Eqn. (3) and (4) the pairwise comparison between different rows of photodetector hatch is performed to provide the similarity matrix $\boldsymbol{S}$ elated to graph $G \equiv (V, E, W)$. Going through the second step, the Laplacian matrix of graph $\boldsymbol{\mathcal{L}}$ is constructed using Eqn. (7). Then the first 10 $(= n)$ non-zero Laplacian Eigenvectors $\boldsymbol{v}_i, i = \{2 \ldots 11\}$ are used to build a spectral universal basis $\boldsymbol{\mathcal{V}}_{normal}$ necessary for spectral transformation (Eqn. (10)). Next, the spectral graph Fourier coefficients ($\boldsymbol{C}$) are obtained by taking the inner product $\left(\boldsymbol{x}_l^p\right)^T (\boldsymbol{\mathcal{V}}_{normal})$ per Eqn. (12).

Finally, the coefficients of $\boldsymbol{C}$ are traced on a Hoteling T^2 control chart. Per the procedure for building the Phase 1 control chart described in Step 4.1, the upper control limit (UCL) is first estimated by only considering the so-called in-control signal, viz., those layers not contaminated with tungsten or aluminum particles. As mentioned previously, this was restricted to 24 of the 60 layers for the first iteration of the build with 100 hatches per layer. The T^2 statistic and the upper control limit (UCL) are calculated based on Eqn. (13) and (14).

The Phase 1 spectral graph theoretic Hoteling T^2 control chart along with the data for the six level of tungsten and aluminum contamination for the first iteration is shown in Figure 11. There are a total of 6000 hatches (60 layers) for which the data is available in the first iteration. Each point of the control chart is representative of the spectral graph coefficients for one hatch. It is observed that the chart captures the occurrence of contamination almost instantaneously. The Type I error for tungsten and aluminum in building the Phase 1 control chart was found to be ≈ 0.3% and 0.7%. After revising the control limit by applying the delete and revise procedure once, the Type I error rate reduced to ≈ 0.1%.

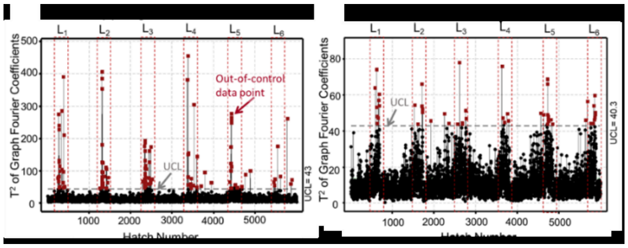

Figure 11: The Phase 1 spectral Hoteling T2 control chart related to six levels of contamination for (a) Tungsten and (b) Aluminum contamination, wherein the control limits are fixed.

Next, following the procedure in Step 4.2, the Hoteling T^2 chart is used to detect contamination in the rest of the two experimental iterations of the build. The data is representative of 120 layers, with each layer having 100 hatches for a total of 12,000 hatches. To plot the spectral control chart for the other replicates, the upper control limit (UCL) stays identical from Phase 1 in Figure 11. As new data $\boldsymbol{y}$ arrives, it is multiplied with the universal basis $\boldsymbol{\mathcal{V}}_{normal}$ to extract the first ten spectral graph Fourier coefficients $\widehat{G}(\boldsymbol{y})$ as shown in from Eqn. (15).

Subsequently, T_y^2 is obtained in Eqn. (16), and plotted on the control chart. This simple inner product makes this approach suitable for online monitoring. Figure 12 shows the application of the Phase 2 control chart to each type of contamination. Every level of tungsten contamination is detected promptly detected by the control chart in Figure 12 (a), whereas, the aluminum contamination level L_5 is missed (an example of Type II error).

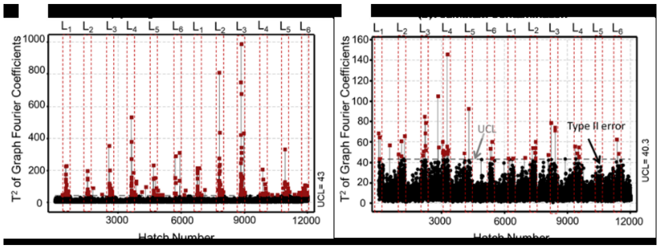

Figure 12: The Phase 2 spectral Hoteling T2 control chart applied to two replications of the data for the related to the remaining two iterations, for each of the six levels of contamination for (a) tungsten and (b) aluminum contamination.

Table 2 summarizes the Type I and Type II errors estimated from three replicates of the experiment in detecting powder contamination. We note that because it is intractable to pinpoint *a priori* the exact hatch where contamination has occurred, the Type II errors are reported in terms of all the hatches for the entire layer where contaminants are added. In contrast, it is known for certain whether a hatch belongs to a non-contaminated layer, hence the Type I error can be localized with respect to every hatch.

The results from the proposed approach are compared with traditional delay-embedded stochastic models, such as autoregressive (AR), autoregressive moving average (ARMA), and autoregressive integrative moving average (ARIMA) models. Starting with the simplest model with two autoregressive terms, the model search is stopped when the number of terms in the model reaches 10. The stopping criteria is chosen so that the number of terms in the most complicated model does not exceed the number of eigenvectors (n =10) used in the spectral graph theoretic approach.

For each model, the Hoteling T^2 control chart is constructed and the Type I and Type II errors are estimated using the same procedure used for the proposed spectral graph theoretic approach. The Phase 2 results for the traditional stochastic time series methods are presented in Table 2, from which it is evident that the onset of material cross-contamination is promptly detected in the case of tungsten contamination; the Type II (β) error rate is negligible for tungsten contamination and the Type I (α) error is less than 1% for a majority of cases. However, detection of aluminum contamination is rather intractable with existing approaches; the Type II error exceeds 10%. The results depicted in Table 2 also provide the average computation time for extracting the T^2 values for one hatch in the Phase 2 part of the control chart. The computation time for the proposed approach is less than a millisecond (~ 0.8 millisecond), which is magnitude smaller in comparison to traditional approaches. Thus, attesting to the viability of the approach for real-time process monitoring in AM.

Table 2: The algorithm accuracy in comparison with traditional approaches for detecting the Tungsten and Aluminum contamination. The numbers in the parenthesis are from three-fold experimental replications.

Aluminum Contamination			
Model Structure	Type I error (%)	Type II error (%)	Computation Time (Per hatch, sec)
ARMA (4,6)	0.8 (0.2)	66.7(16.7)	0.1302
ARMA (6,4)	1.7 (0.1)	16.7 (9.2)	0.2829
ARIMA (4,6)	1.1 (0.0)	66.7(16.7)	0.1560
ARIMA (6,4)	1.6 (0.1)	11.1 (9.6)	2.4152
AR (10)	0,5 (0.1)	33.3 (17)	0.8641
Stat Features	1.5 (0.0)	11.1 (9.6)	0.0427
Proposed Approach	0.5 (0.0)	5.0 (9.2)	0.0008
Tungsten Contamination			
Model Structure	Type I error (%)	Type II error (%)	Computation Time (Per hatch, sec)
ARMA (4,6)	1.2 (0.0)	0.0 (0.0)	0.1302
ARMA (6,4)	1.0 (0.1)	0.0 (0.0)	0.2829
ARIMA (4,6)	1.2 (0.1)	0.0 (0.0)	0.1560
ARIMA (6,4)	1.6 (0.1)	0.0 (0.0)	2.4152
AR (10)	0.8 (0.2)	0.0 (0.0)	0.8641
Stat Features	1.3 (0.7)	0.0 (0.0)	0.0427
Proposed Approach	1.1 (0.1)	0.0 (0.0)	0.0008

3.3 Verification with XCT

Continuing with the analysis, since the position data for each hatch of the photodetector signal is available, the spectral graph T^2 coefficients can be correlated with the layer-by-layer contamination pattern obtained from the CT scan. Such an attempt is made in Figure 13 for the tungsten contamination case. In Figure 13(a), the Hoteling T^2 values for the spectral graph coefficients are color coded, with red indicating out-of-control or contaminated hatches, and black representing the nominal (contamination-free) condition. The coefficients are superimposed on the XCT of the specimen taken along the X-Z cross-section in Figure 13(b); the XCT is along the cutting plane B-B in Figure 13. From the overlaid plot in Figure 13(b) it is evident that there is a near one-to-one correlation between the sensor signatures and the layer at which contamination occurs.

This result corroborates that the spectral graph sensor signatures are indeed indicative of material cross-contamination and can be traced back to physical locations where contamination is present. This traceability of sensor signatures to XCT demonstrates the viability of the *qualify-as-you-build* paradigm in AM, wherein in-process sensor data instead of cumbersome offline measurement and testing can be used to rapidly qualify the part quality.

Furthermore, through this research, once the presence of contaminants is discovered at a layer, measures to forestall further their spread over future layers can be taken. Such a preventive strategy could be, for instance, rescanning an entire layer with higher energy density to ensure thorough fusion of contaminant particles like tungsten. In the worst-case scenario, the build can be stopped to prevent poor quality builds and waste of expensive powder.

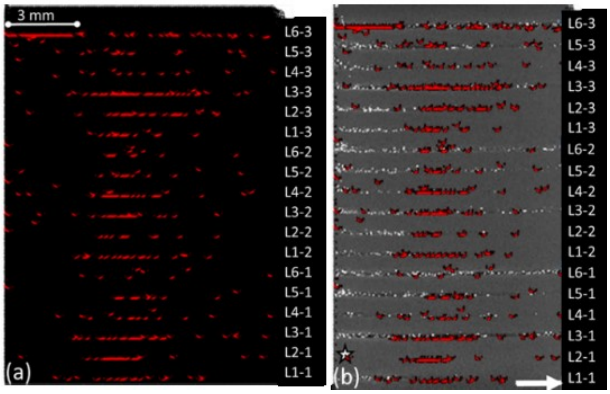

Figure 13: (a) The T^2 values of the spectral graph Fourier coefficients are color coded, red indicates out-of-control (contaminated) hatches, and black indicates in-control hatches. These T^2 values are plotted along the X-Z plane of the part, since the position

4 Conclusions and Future Work

This work describes a spectral graph theoretic approach to detect occurrence of material cross-contamination in laser powder bed fusion (L-PBF) additive manufacturing process (AM) based on in-process sensor data. The key idea is to convert a signal into its network graph equivalent, and subsequently extract so-called spectral graph Fourier coefficients as surrogate signatures to track the process hatch-by-hatch. A photodetector signal is specifically used to demonstrate the efficacy of the approach in L-PBF of Inconel 625 alloy, in which are induced two types of foreign material contaminants, namely, tungsten and aluminum varying in the severity and the manner in which they are introduced (static deposition, and dynamic/continuous deposition over a layer).

The key advantages of the approach over existing time-delay stochastic time series modeling techniques, such as autoregressive moving average (ARMA) is that: (a) it does not require fitting a model to the data, essentially it is model-free; and (b) eschews decomposition or extraction of features from each incoming signal, a simple inner product with a eigenvector basis is required thus saving on computational time. As a result, the approach detects instances of material contamination with high accuracy (worst case Type I error < ~1%, and Type II error < 5%), which is magnitude improvement over traditional time series modeling. The ability to detect contamination was corroborated with offline metallurgical and X-ray computed tomography (XCT) scanning.

A major drawback of this work is that uses only a single type of sensor – a photodetector – to detect a specific type of defect, namely, material cross-contamination. The efficacy of the approach using multiple sensors for different types of defects remains to be ascertained. Furthermore, the type and severity of contamination could not be isolated based on data from a single photodetector, and the effect of contamination on the mechanical properties needs to be quantified through materials testing. This will allow completing the loop between process phenomena, sensor signatures, and part properties. The authors will attempt to address these gaps in their future work in the area.

Acknowledgements

This work is supported in part by the following National Science Foundation grants CMMI-1719388, CMMI-1739696, and CMMI-1752069 (CAREER).

References

[1] Shinbara, T., 2013), "Additive manufacturing: Enabling advanced manufacturing," NAE Convocation of the Engineering Professional Societies, National Academy of Engineering, Washington DC.

[2] Lewandowski, J. J., and Seifi, M., 2016, "Metal additive manufacturing: a review of mechanical properties," Annual Review of Materials Research, 46, pp. 151-186

[3] Gorelik, M., 2017, "Additive manufacturing in the context of structural integrity," International Journal of Fatigue, 94(2), pp. 168-177.doi:https://doi.org/10.1016/j.ijfatigue.2016.07.005

[4] Sharratt, B. M., 2015, "Non-destructive techniques and technologies for qualification of additive manufactured parts and processes," no. March

[5] Seifi, M., Salem, A., Beuth, J., Harrysson, O., and Lewandowski, J. J., 2016, "Overview of Materials Qualification Needs for Metal Additive Manufacturing," JOM, 68(3), pp. 747-764.doi:10.1007/s11837-015-1810-0

[6] Peralta, A. D., Enright, M., Megahed, M., Gong, J., Roybal, M., and Craig, J., 2016, "Towards rapid qualification of powder-bed laser additively manufactured parts," Integrating Materials and Manufacturing Innovation, pp. 1-23.doi:10.1186/s40192-016-0052-5

[7] Bourell, D., Kruth, J. P., Leu, M., Levy, G., Rosen, D., Beese, A. M., and Clare, A., 2017 (In-Press), "Materials for additive manufacturing," CIRP Annals - Manufacturing Technology.doi:https://doi.org/10.1016/j.cirp.2017.05.009

[8] Sames, W. J., List, F., Pannala, S., Dehoff, R. R., and Babu, S. S., 2016, "The metallurgy and processing science of metal additive manufacturing," International Materials Reviews, 61(5), pp. 315-360

[9] Brandão, A., Gerard, R., Gumpinger, J., Beretta, S., Makaya, A., Pambaguian, L., and Ghidini, T., 2017, "Challenges in Additive Manufacturing of Space Parts: Powder Feedstock Cross-Contamination and Its Impact on End Products," Materials, 10(5), p. 522

[10] Boulware, P., 2016, "Final Technical Report to National Institute of Standards and Technology and National Center for Defense Manufacturing and Machining - Measurement Science Innovation Program for Additive Manufacturing: An Evaluation of In-Process Sensing Techniques Through the Use of an Open Architecture Laser Powder Bed Fusion Platform," No. NIST# 70NANB13H192 - 20140097, Edison Welding Institute (EWI), Cincinnati, OH.

[11] King, W., Anderson, A., Ferencz, R., Hodge, N., Kamath, C., and Khairallah, S., 2014, "Overview of modelling and simulation of metal powder-bed fusion process at Lawrence Livermore National Laboratory," Materials Science and Technology, 31(8), pp. 957-968

[12] Tootooni, M. S., Rao, P. K., Chou, C.-A., and Kong, Z. J., 2016, "A Spectral Graph Theoretic Approach for Monitoring Multivariate Time Series Data from Complex Dynamical Processes," IEEE Transactions Automation Science and Engineering, Accepted - In Press

[13] Shi, J., and Malik, J., 2000, "Normalized cuts and image segmentation," IEEE Transactions on Pattern Analysis and Machine Intelligence, 22(8), pp. 888-905

[14] Chung, F. R. K., 1997, Spectral Graph Theory, American Mathematical Society, Providence, RI.

[15] DeJesús, O., and Hagan, M. T., 2001, "Backpropagation through time for a general class of recurrent network," 11th International Joint Conference on Neural Networks, Washington, D.C., pp. 2638-2642

[16] Sandryhaila, A., and Moura, J. M., 2013, "Discrete signal processing on graphs," IEEE Transactions on Signal Processing, 61, pp. 1644-1656

[17] Montgomery, D. C., 2009, Statistical quality control, Wiley New York.